Revealing the structure of a catalytic combustion active-site ensemble combining uniform nanocrystal catalysts and theory insights

An-Chih Yang[a,b], Tej Choksi[a,b,c] [ID], Verena Streibel[a,b,c] [ID], Hassan Aljama[a,b,c], Cody J. Wrasman[a,b], Luke T. Roling[a,b,c,d] [ID], Emmett D. Goodman[a,b], Dionne Thomas[a], Simon R. Bare[c] [ID], Roel S. Sánchez-Carrera[e], Ansgar Schäfer[f], Yuejin Li[g], Frank Abild-Pedersen[c,1], and Matteo Cargnello[a,b,1] [ID]

[a]Department of Chemical Engineering, Stanford University, Stanford, CA 94305; [b]SUNCAT Center for Interface Science and Catalysis, Stanford University, Stanford, CA 94305; [c]SLAC National Accelerator Laboratory, SUNCAT Center for Interface Science and Catalysis, Menlo Park, CA 94025; [d]Department of Chemical and Biological Engineering, Iowa State University, Ames, IA 50011; [e]Digitalization of Research & Development, BASF Corporation, Tarrytown, NY 10591; [f]Digitalization of Research & Development, BASF SE, 67056 Ludwigshafen, Germany; and [g]Environmental Catalysis R&D, BASF Corporation, Iselin, NJ 08830

Supported metal catalysts are extensively used in industrial and environmental applications. To improve their performance, it is crucial to identify the most active sites. This identification is, however, made challenging by the presence of a large number of potential surface structures that complicate such an assignment. Often, the active site is formed by an ensemble of atoms, thus introducing further complications in its identification. Being able to produce uniform structures and identify the ones that are responsible for the catalyst performance is a crucial goal. In this work, we utilize a combination of uniform Pd/Pt nanocrystal catalysts and theory to reveal the catalytic active-site ensemble in highly active propene combustion materials. Using colloidal chemistry to exquisitely control nanoparticle size, we find that intrinsic rates for propene combustion in the presence of water increase monotonically with particle size on Pt-rich catalysts, suggesting that the reaction is structure dependent. We also reveal that water has a near-zero or mildly positive reaction rate order over Pd/Pt catalysts. Theory insights allow us to determine that the interaction of water with extended terraces present in large particles leads to the formation of step sites on metallic surfaces. These specific step-edge sites are responsible for the efficient combustion of propene at low temperature. This work reveals an elusive geometric ensemble, thus clearly identifying the active site in alkene combustion catalysts. These insights demonstrate how the combination of uniform catalysts and theory can provide a much deeper understanding of active-site geometry for many applications.

catalyst | nanocrystal | theory | combustion | active site

Supported metal catalysts are widely used in many industrial and environmental processes (1). Typically, these catalysts are prepared by deposition of molecular precursors on high surface area supports in order to increase the metal fraction exposed to reactants, thus leading to the formation of small nanoparticles (NPs). During the synthesis process, a wide variety of surface structures may be formed, and not all of them may be active for the reaction of interest. This heterogeneity complicates the identification of the active sites, a crucial piece of information to develop synthesis methods to produce them with the largest possible density. In order to find the catalytic active sites, a reductionist approach is useful to disentangle multiple parameters that are present in industrial catalysts (2). This reductionist approach benefits from combining theory, experiments, and characterization to identify active sites (3), a long-standing challenge in the field. The beneficial outcome of developing this fundamental understanding is in the possibility to produce higher-performing catalysts for commercial applications.

An area where catalyst improvements must be continuously made is that of vehicle exhaust catalysts, given the advances in low-temperature combustion engines and stricter engine emission regulations that demand continued reductions in atmospheric pollutants (mainly hydrocarbons, carbon monoxide, and nitrogen oxides) (4). These catalysts are required to operate at lower temperatures than what is currently achieved, and therefore finding materials that provide higher rates below ∼500 °C is imperative. Despite tremendous efforts that have led to remarkable achievements in this technology, further improvements are necessary for several transportation sectors (trucks, ships) that are unlikely to be electrified in the immediate future (5). Hydrocarbons, including propylene (or propene), are some of the most abundant pollutants emitted into the atmosphere with strong photochemical ozone formation potential (6). Propene has a strong carbon–carbon double bond, and it shows stronger binding to metal surfaces compared to alkanes (7). Understanding the material's structural requirements for increased activity and stability in propene combustion is useful to design better-performing emission control catalysts.

Most current oxidation catalysts use Pt and Pd since these elements are known for their high efficiency and stability (8, 9). Despite the large amount of work, there is no consensus on a detailed atomistic understanding of the active site. One factor

CHEMISTRY

Significance

Catalysts are essential for a sustainable future because they reduce the energy required in chemical processes and the emission of harmful and polluting compounds. Revealing the function and structure of a working catalyst is a challenging task but critical in order to prepare more efficient and higher-performing materials. Very often, active sites are formed by many atoms that cooperate to perform the catalytic function. It is therefore challenging to identify the structure of the active site. Here, we combine uniform nanocrystal catalysts and theory insights to reveal the active-site ensemble necessary for alkene combustion. This approach can be extended to reveal atomistic details of working catalysts for a variety of applications.

that complicates the comparison is that conventional catalyst preparation results in ill-defined metal sizes and compositions, making it hard to reveal the active sites. In the case of propene, studies report differing arguments and explanations. Some researchers recently observed a decrease in turnover frequency (TOF) at larger Pt average particle size (10, 11). In the past, an opposite trend was observed instead (12), where researchers claimed that propene is more readily oxidized on terrace sites rather than on kinks and edges because the binding of O_2 and propene molecules is too strong on undercoordinated sites, in line with additional recent work (13). Similar trends have also been observed on Pd/Al_2O_3 catalysts, but different explanations were provided, such as the higher fraction of Pd(0) in the samples with larger Pd particle size (14). However, there are reports about the importance of step-edge motifs on Pd, Pt, and Ni for alkene decomposition (15–18). It is thus questionable whether terrace atoms are truly the active sites on Pd and Pt catalysts. One further element complicating this picture is that in most studies in the literature, water is not used in the reaction mixture despite its known inhibiting effect (19–21). It is crucial to know the structure of catalytic active sites with precision to optimize the use of noble metals under relevant reaction conditions.

In the present work, we report the systematic identification of the geometric active-site ensemble responsible for determining the high performance of Pt-based catalysts for propene combustion. By using a combination of uniform nanocrystal catalysts and theory insights, we demonstrate that larger particle sizes give rise to higher TOFs, thus showing that the reaction is mildly structure sensitive. Water has beneficial effects in producing a larger fraction of step sites. In combination with theoretical calculations, we demonstrate that these ensembles of step-edge sites with specific coordination numbers (CNs) are the active sites. More generally, we demonstrate that combining uniform catalysts and theoretical insights is invaluable in providing us with a clear picture of active sites in catalyzed reactions.

Results and Discussion

Initial studies were performed on small and uniform Pd/Pt bimetallic NPs prepared using previously reported methods (22) that allowed us to tune the Pd/Pt atomic ratio (3/1, 1/1, and 1/3) (*SI Appendix*, Fig. S1). The as-synthesized NPs were deposited on thermally stable supports of industrial relevance ($W_{0.04}Ti_{0.96}O_{2.04}$; $Mn_{0.3}Zr_{0.7}O_{1.7}$; $Mn_{0.65}Cu_{0.35}O_{1.65}$; CeO_2; and $\gamma\text{-}Al_2O_3$) to explore their role. The total amount of active metal (both Pd and Pt) was chosen to be 0.94 at% for all catalysts, such that each sample nominally contained the same number of Pd and/or Pt metal atoms, or a combination thereof. Ligands on the supported NPs were removed through a fast thermal treatment using previously reported procedures (23) without affecting size and size distributions (*SI Appendix*, Fig. S1 *F–O*). The metal composition in the supported catalysts was confirmed by inductively coupled plasma–optical emission spectroscopy (ICP-OES) (*SI Appendix*, Table S3). Despite small variations in the weight loadings from the desired values, the samples represent a library of catalysts, in which the composition is the only variable across the series.

We screened the performance of the catalysts for propene combustion. Initially, light-off curves were recorded under lean conditions (oxygen-to-propene ratio of 20) both in the absence and presence of steam (10 vol%) on alumina-supported samples (*SI Appendix*, Fig. S2A). We obtained two main results: First, we found the lowest temperature for complete combustion of propene, with or without steam, for the samples with intermediate composition (Pd/Pt 1/1) (*SI Appendix*, Fig. S2 *A and B*). Second, the addition of 10 vol% steam caused a general decrease in catalytic activity, with temperatures for complete conversion increasing for all of the catalysts except for Pt (*SI Appendix*, Fig. S2 *A and B*), as measured by the temperature to achieve 50% propene conversion (denoted as T_{50}). It is known that Pd catalysts

are heavily affected by steam in combustion processes (24); surprisingly, this was not the case for the Pt sample. The same trend of metal compositional effect was observed on all other supports (*SI Appendix*, Fig. S3), further corroborating the idea that support effects did not outweigh the compositional effect. Alumina produced the most active samples across all of the supports studied. We believe that differences in metal dispersion and the presence of monometallic and alloyed phases in catalysts prepared by conventional impregnation are responsible for ambiguous support effects in previous work (25–27). Alumina-supported catalysts were then the only focus in this study because of the potential to give the most active catalyst.

Kinetic measurements were performed under steady-state conditions and strict kinetic control (see calculations of external and internal mass transport limitations in *SI Appendix*) after catalysts reached stable rates. An initial limited deactivation trend was observed and attributed to likely reconstruction and oxidation changes on the surface of the catalysts (*SI Appendix*, Fig. S4A), which however did not corrupt the trends and conclusions from the kinetic analysis. The trends observed in kinetic studies matched those obtained from light-off experiments (*SI Appendix*, Fig. S2C). Values of the apparent activation energy for the samples confirmed a beneficial trend with Pt-containing samples showing a decreased activation energy in the presence of steam (*SI Appendix*, Fig. S2D). The samples were reduced before recording the rates, and it was observed that >3 h were required to reach steady state on the pure Pd sample, whereas the pure Pt sample showed stable rates immediately after both reducing and oxidizing treatments (*SI Appendix*, Fig. S5). We hypothesize that this behavior is due to the slow oxidation of the Pd phase (28). Although the metallic phase appeared initially more active, the oxidizing atmosphere caused surface oxidation of Pd that precluded the utilization of metallic Pd in practical conditions. TOFs (*SI Appendix*, Fig. S2E) were calculated using rate measurements normalized by exposed Pd and Pt surface area measured by CO chemisorption on the reduced samples. It was observed that Pd/Pt alloys showed higher TOFs than pure Pd and Pt, probably because Pd was maintained in metallic state by alloying with Pt, and metallic Pd from reductive treatment is more active than Pt (*SI Appendix*, Fig. S5). As for the water effect, pure Pd and 3/1 Pd/Pt catalysts showed higher TOFs in the absence of steam, confirming that Pd-rich catalysts are more sensitive to water poisoning (24, 29). Surprisingly, the trend was reversed on Pt-rich samples: Their TOFs were equal (for Pd/Pt 1/1) or higher (for Pd/Pt 1/3 and pure Pt) in the presence of water, and the TOF improvement linearly increased with increasing Pt content (*SI Appendix*, Fig. S2F). We will elaborate on the reasons for this behavior further below. Although the water enhancement was not observed in T_{50}, which is a non–steady-state measurement, it helped demonstrate a comprehensive picture, particularly on Pt-rich catalysts, with a convincing trend in the ΔT_{50} (the difference in T_{50} in the presence of steam and T_{50} in its absence) observed varying from the pure Pd sample (ΔT_{50} of −35 °C) to the pure Pt sample (ΔT_{50} of +1.5 °C).

We then set out to understand the effect of particle size on the performance of the catalysts, thus allowing us to identify which exposed sites are the most active (30, 31). A new library of catalysts was prepared with a fixed bimetallic Pd/Pt 1/1 composition chosen to represent a compromise between the activity and behavior of the two pure metals. A seed-mediated and in situ alloying approach was employed to synthesize NPs of different sizes, leading to a final nanocrystal library with sizes of 2.3, 3.8, 4.6, 7.3, and 10.2 nm. The nanocrystals were deposited on the same alumina used above and the ligands removed by the same fast thermal treatment. Representative transmission electron microscopy (TEM) images of the starting and supported NPs demonstrate the uniformity of the Pd/Pt bimetallic catalysts (Fig. 1).

CO chemisorption experiments further corroborated the change in particle size across the library, with the fraction of exposed Pd or Pt atoms decreasing as the particle size increased (*SI Appendix*, Table S4), with the assumption that both Pd and Pt atoms adsorbed CO with the same stoichiometry. ICP-OES confirmed that the Pd/Pt ratio was close to 1/1 across samples, with small variations (*SI Appendix*, Table S4). To further demonstrate that the NPs remained alloyed after ligand removal and catalysis, characterization including Pd extended X-ray absorption fine structure (EXAFS) at the K-edge and scanning transmission electron microscopy (STEM) in combination with energy-dispersive X-ray spectroscopy (EDS) was performed on Pd/Pt 1/1 NPs supported on Al_2O_3 (Fig. 2 and *SI Appendix*, Table S5 and Fig. S6). EXAFS data (Fig. 2A) illustrate trends in the Pd CNs with Pd, Pt, and O as a function of Pd/Pt nanocrystal size in the supported samples and show that all of the bimetallics have Pd–Pt CNs slightly higher than Pd–Pd (Fig. 2B and *SI Appendix*, Table S5). The values agree with previously reported work on small Pd/Pt nanocrystal catalysts and demonstrate the formation of Pd/Pt alloys (22), where at least half of the neighboring Pd atoms are replaced by Pt atoms. X-ray absorption near-edge spectroscopy (XANES) data show that small particles are more oxidized compared to larger ones (Fig. 2C). It is likely that oxidized Pd is located close to the surface of the nanocrystals. Nevertheless, the degree of alloying is still large since the Pd–Pt scattering path of all of the samples (*SI Appendix*, Table S5) is at bonding distance (2.74 Å, the bond length of Pd atoms in metallic Pd) (22, 32), and it is conserved across the different particle sizes. Finally, STEM-EDS mapping and line scan analysis were performed on 10.2-nm Pd/Pt 1/1 NPs and Pd-K and Pt-L$_3$ signals were found to be evenly distributed across the whole particle (Fig. 2 D–F and *SI Appendix*, Fig. S6), thus further supporting that the bimetallic NPs are alloyed. Since this sample represents the largest Pd seed size that was used for the synthesis, it is reasonable to hypothesize that kinetic barriers for alloying are even smaller for the other samples where the Pd seed size is smaller. Overall, the characterization supports the alloy nature of the Pd/Pt catalysts with different particle sizes.

Reaction rates for propene combustion were measured under steady-state conditions once samples stabilized both in the absence and presence of steam (*SI Appendix*, Fig. S4B) and normalized by the available exposed atoms according to CO chemisorption data (Fig. 3A). We observed that catalysts with larger size showed higher TOFs, up to approximately five times between the 10.2- and the 2.3-nm Pd/Pt catalysts. This trend is in line with previous studies (10, 12–14), revealing that propene combustion is mildly structure sensitive. There are currently several opposing explanations for this phenomenon. Interestingly, the apparent activation energy values were very similar for all catalysts within measurement error (Fig. 3B), suggesting that the samples share the same active site but that their number increases moving from smaller to larger NPs, despite the decrease in exposed surface atoms.

In order to further unravel the details of the structure sensitivity of the Pd/Pt catalysts, we measured reaction rate orders under steady-state conditions for propene, oxygen, and water for the library of catalysts with different compositions and different particle sizes. No significant deactivation or induction period was observed during changes in partial pressure of reactants (*SI Appendix*, Fig. S4C), which assured that reliable TOFs reflected stabilized surface properties of different samples. The rate order for CO_2 was measured to be zero (*SI Appendix*, Fig. S7), indicating the product desorption does not limit the reaction. The results for the rate orders for the other species show that consistent trends emerge across all of the samples studied.

For the series of catalysts with constant small particle size and varying composition (*SI Appendix*, Fig. S8 A–C), the propene reaction order is mildly negative (from −0.2 to −0.5, *SI Appendix*, Fig. S8A) for all of the samples, whereas the oxygen reaction order is positive (between 0.85 and 1.1, *SI Appendix*, Fig. S8B), indicating propene's stronger adsorption and higher coverage on the NP surface than those of oxygen. Interestingly, differences in the water rate order were found, with the Pd/Al_2O_3 catalyst showing negative reaction order (−0.5, *SI Appendix*, Fig. S8C), whereas its Pt counterpart showed a positive order (0.3). Samples with intermediate compositions between the two extremes showed a gradual change in the water reaction order from pure Pd to the pure Pt sample values. The water rate order observation is in agreement with the beneficial effect of water displayed in light-off curves by the Pt catalyst (*SI Appendix*, Fig. S2). This trend suggests that water is responsible for poisoning Pd sites, but surprisingly also for improving the activity of Pt surfaces. The water rate order is in line with the water effect in *SI Appendix*, Fig. S2 C–F where the presence of water resulted in lower TOFs in Pd and Pd-rich
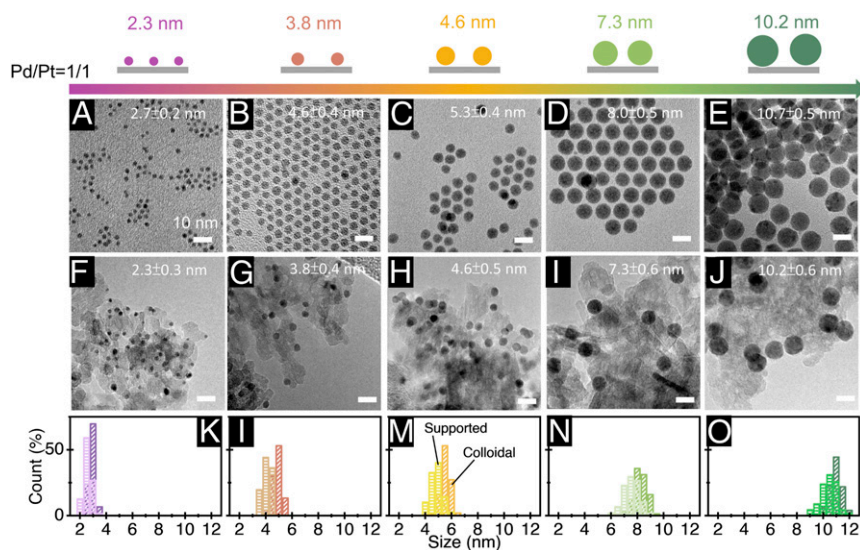

Fig. 1. (A–E) Representative TEM images of bimetallic Pd/Pt of fixed composition (1/1 atomic ratio) and increasing size; and (F–J) after their deposition onto alumina and ligand removal. K–O report particle size distributions of pristine nanocrystal in colloidal solution (diagonal line patterned) and on alumina support (horizontal line pattern).
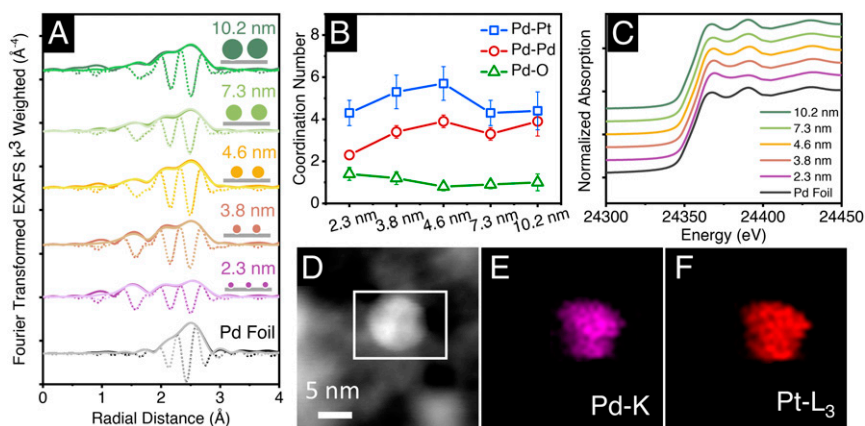
Yang et al.

Fig. 2. (*A*) Fourier transform EXAFS at the Pd K-edge with model fits where the darker lines represent data, the faded lines represent best-fit models, the solid lines represent Fourier transform magnitude, and the dotted lines represent the imaginary component of the Fourier transform. (*B*) CN of Pd–Pd, Pd–Pt, and Pd–O on fresh supported Pd/Pt = 1/1 NPs with different sizes and (*C*) Pd K-edge XANES. (*D*–*F*) STEM-EDS mapping on supported 10.2-nm Pd/Pt NPs.

samples, but higher TOFs in Pt and Pt-rich samples. Other work reports a positive effect of water on platinum-rich samples for propene combustion (29); however, the beneficial effect of water is related to the removal of residual by-products from the synthesis (e.g., chlorine) that are not present in our catalysts. In this work, we show that water plays a different role.

With respect to the size effects on reaction orders for the Pd/Pt 1/1 catalysts, more interesting trends were discovered (Fig. 3 *C*–*E*). The propene rate order became progressively more negative as the Pd/Pt nanocrystal size was increased, varying from −0.5 to −1.2 (Fig. 3*C*) and signifying a stronger binding of propene to the surface of larger Pd/Pt NPs. We believe this effect is due to different active sites that bind propene more strongly and determine the increased reactivity of the samples. In line with this element, an increase in the reaction order for oxygen from 1.0 to 1.3 was observed as the Pd/Pt size was increased (Fig. 3*D*). These values show that as the propene coverage becomes higher on larger particles, oxygen requires higher pressures to bind and activate, suggesting that competitive adsorption takes place. Finally, the water reaction order was only mildly affected by a change in

particle size (Fig. 3*E*). This observation suggests that water adsorption only depends on the chemistry (i.e., different metal type), rather than the geometry (i.e., different sites) of the surface sites. This result in turns confirms that there is no drastic variation in surface chemical composition between samples having different particle sizes.

Before discussing more in detail the effect of reaction conditions on the structure of catalysts with different particle sizes, we confirmed that the particle sizes were maintained before and after catalysis (*SI Appendix*, Fig. S9 and Table S6), and no segregation of the metals was observed after catalysis (see postcatalysis EDS-mapping in *SI Appendix*, Fig. S10). X-ray photoelectron spectroscopy also demonstrates that there was no change in oxidation state before and after catalysis, as Pd was present in its metallic state in both cases on Pd/Pt samples with different particle sizes (*SI Appendix*, Fig. S11). Reconstruction of the particle surface occurred under reaction conditions (see below); however, it is unlikely that any surface area change is so dramatic as to drastically modify the trends and the catalytic rates reported
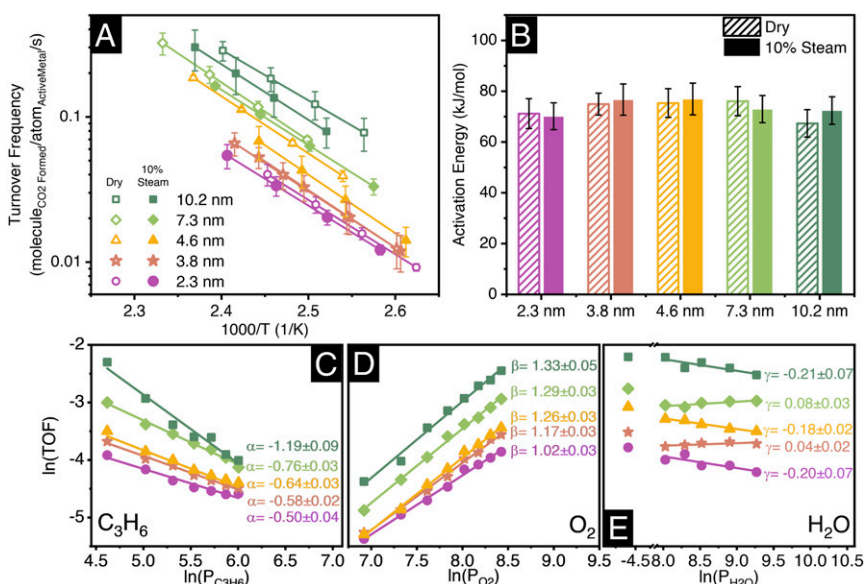

Fig. 3. (*A*) TOF and (*B*) apparent activation energy for propene combustion on supported Pd/Pt NP catalysts with varying size from 2.3 to 10.2 nm. Rate order for (*C*) propene, (*D*) oxygen, and (*E*) water in Pd/Pt/Al$_2$O$_3$ 1/1 catalysts with different sizes.

Yang et al.

as TOF in Fig. 3 given that particle size is very well maintained (*SI Appendix*, Fig. S9).

Prior studies of propene oxidation have explained the higher TOFs observed for larger NPs by the increase in the fraction of terrace sites using truncated cuboctahedra that expose (100) and (111) facets as representations of the NP shape (12, 13). In a postcatalysis TEM characterization of our 10.2 nm Pd/Pt/Al$_2$O$_3$ sample, however, we found spherically shaped NPs (see below). This finding disagrees with the previously assumed, highly faceted cuboctahedral NPs exposing only (111) and (100) terrace sites. A possible reason for this discrepancy in shape is that these previous studies did not explicitly consider how the reaction atmosphere influences the particle shape. Adsorbates are known to change surface energies of certain facets (33–35). Hence, cuboctahedra might not be a proper representation of the NP shape under reaction conditions. The seemingly counterintuitive trend of larger NPs showing higher fractions of undercoordinated sites on the surface is possible because the reaction environment contains adsorbates that stabilize these sites by strong binding (33, 34).

To elucidate the reason for the observed spherical shape of the Pd/Pt NPs under reaction conditions and to identify structural motifs correlating with propene oxidation activity, we turned to density functional theory (DFT)-derived Wulff constructions. In vacuum, our theoretical morphology analysis indicates that Pd/Pt NPs are predominantly composed of terrace sites (Fig. 4*A*). In the presence of water (at 423 K and represented by the equilibrium 1/1 p$_{H2}^{0.5}$/p$_{H2O}$), however, Wulff constructions reveal much more spherical Pd/Pt NPs (Fig. 4*B*), indicating that the OH binding to the surface atoms stabilizes undercoordinated sites (*SI Appendix*, Fig. S12*A*), and further corroborating the postcatalysis TEM characterization (Fig. 4*C*). Based on the spherical NP morphology noted by both experiments and theory, we therefore hypothesize that the structure sensitivity of propene combustion is not related to the increased number of terrace sites in larger particles, as indicated in prior reports (12, 13), but that other active-site ensembles emerge during propene combustion. Although the Wulff construction in Fig. 4*A* is generated using surfaces having a molar ratio of Pd/Pt of 1/1, we will subsequently show that the broad structural trends are independent of the surface composition.

Using ab initio thermodynamics, we calculated the ratios of surface energies of terminations exposing undercoordinated sites to terrace-like terminations exposing sites having higher coordinated sites. We employed (211) and (110) surface terminations as proxies for undercoordinated edge sites, and (111) and (100) terminations as surrogates for higher-coordinated terraces.
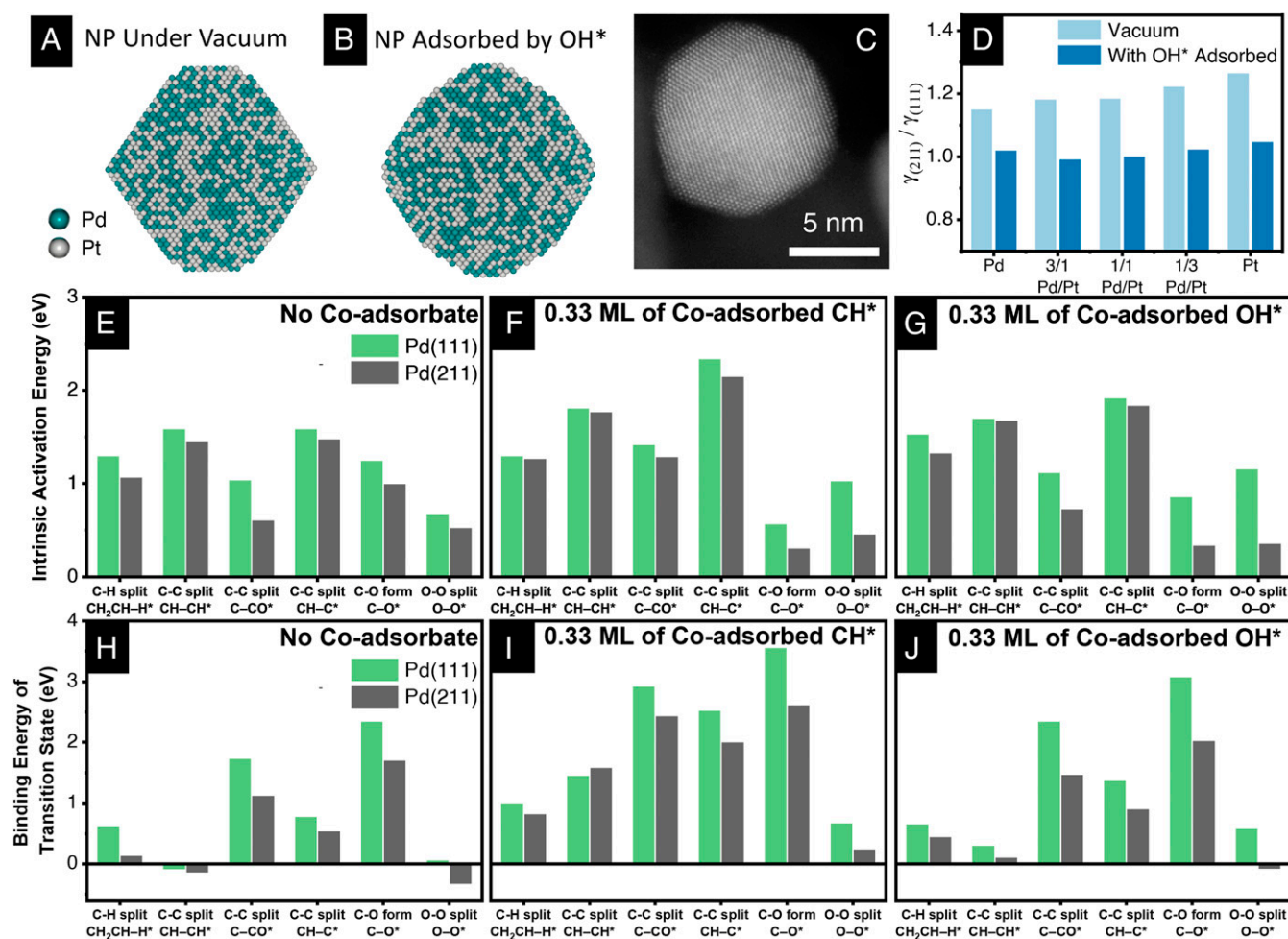
Fig. 4. Simulated Pd/Pt (atom ratio 1/1) particle shape from the [110] direction in vacuum (*A*) and with steam (*B*). (*C*) Postcatalysis TEM image of 10.2-nm NP with Pd/Pt = 1/1 on Al$_2$O$_3$. (*D*) Ratio of surface energy between (211) and (111) surfaces [γ$_{(211)}$/γ$_{(111)}$] on NPs with different Pd/Pt ratios. Intrinsic activation barriers of representative reactions on Pd(211) and Pd(111) (*E*) without coadsorbates, (*F*) with 0.33 ML of coadsorbed CH*, and (*G*) with 0.33 ML of coadsorbed OH*. Binding energies of transition states on Pd(211) and Pd(211) (*H*) without coadsorbates, (*I*) with 0.33 ML of coadsorbed CH*, and (*J*) with 0.33 ML of coadsorbed OH*.

Yang et al.

These surface energy ratios are determined for alloys ranging from Pd-rich to Pt-rich and these ratios are calculated in both vacuum and in the presence of water. The results shown in Fig. 4D and *SI Appendix*, Fig. S12 indicate that all of the ratios of surface energies [$\gamma_{(211)}/\gamma_{(111)}$, $\gamma_{(100)}/\gamma_{(111)}$, and $\gamma_{(110)}/\gamma_{(111)}$] in vacuum are greater than 1. The ratios in vacuum suggest that surfaces exposing undercoordinated sites are less stable in comparison with terraces, resulting in highly faceted Wulff-constructed NPs (Fig. 4A).

In the presence of cofed water, using site-specific scaling relations (36), we determined the adsorption energies of OH* on Pt and Pd sites having different CNs and wide-ranging Pt:Pd molar ratios (additional details provided in *SI Appendix*). We found that OH* generally adsorbed more strongly on Pt than on Pd. Furthermore, undercoordinated sites (CN: 7) located on (211) surfaces bound OH* more strongly than terrace sites on (111) surfaces. Thus, OH* stabilizes (211) surfaces to greater extents in comparison with (111) surfaces, resulting in significantly lower values of $\gamma_{(211)}/\gamma_{(111)}$, some of which are even slightly below 1 (Fig. 4D). This decrease in $\gamma_{(211)}/\gamma_{(111)}$ caused by OH* adsorption is consistently observed regardless of the Pd/Pt molar ratio on the surface. We have also considered the sensitivity of $\gamma_{(211)}/\gamma_{(111)}$ to any changes in the Pd/Pt molar ratio of the surface layer that may be induced by OH* adsorption. As shown in *SI Appendix*, Tables S18–S21, $\gamma_{(211)}/\gamma_{(111)}$ is generally insensitive to the local surface composition and remains consistently lower in the presence of OH* when the widest latitude of atomic segregation is considered. We observed $\gamma_{(211)}/\gamma_{(111)}$ values that are similar to Fig. 4D upon varying the assumed $p_{H2}^{0.5}/p_{H2O}$ ratio (1/1 in Fig. 4D) from 100:1 to 1:100 (*SI Appendix*, Figs. S39 and S40). In Fig. 4D, $\gamma_{(211)}/\gamma_{(111)}$ is calculated by considering an OH* coverage of 0.25 monolayer (ML). Similar trends in $\gamma_{(211)}/\gamma_{(111)}$ are obtained for OH* coverages between 0.11 and 0.67 ML as shown in *SI Appendix*, Fig. S42. The ratios of surface energies [e.g., $\gamma_{(211)}/\gamma_{(111)}$] determined using DFT agree with surface energies predicted using a coordination-based alloy stability model, validating our computational approach (37). Taken together, the ab initio thermodynamic analysis demonstrates that (211) surfaces exposing undercoordinated sites are stabilized to a greater extent under conditions simulating cofed water compared to vacuum. The undercoordinated sites are known to promote a variety of bond dissociation reactions important for olefin combustion (15–18). The reason why the surface restructuring is stronger for Pt-rich or pure Pt NPs may be related to the oxidation of Pd, which counterbalances the improvement in reactivity due to the effect of steam on undercoordinated sites (*SI Appendix*, Fig. S5). These differences between Pt and Pd are corroborated by the water reaction orders as a function of composition (*SI Appendix*, Fig. S8), which show that water promotes the Pt-rich samples' activity, but not the Pd-rich samples' activity.

To further prove that undercoordinated sites are active sites for propene combustion, we compared DFT-derived activation energies for representative C–H, C–C, O–O bond scission, and C–O bond formation reactions on (111) terraces and (211) step edges. These reactions are part of the propene combustion reaction network. Propene combustion involves numerous elementary steps and identifying a full reaction mechanism is challenging. Here, we focus on the reconstruction of the metal surfaces leading to a larger fraction of specific active sites that are involved in the most important bond-breaking steps. Trends in activation barriers across these classes of reactions provide valuable insights regarding the relative reactivity of steps versus terrace sites. Since rate order measurements imply that the surface contains coadsorbed C_xH_y species (negative propene rate order) and OH_x species (near-zero rate order), we calculated transition state barriers in the presence of 0.33 ML of CH* and 0.33 ML of OH* (see *SI Appendix*, Figs. S13–S25 for the structure of coadsorbates). In addition to reporting intrinsic reaction barriers, we also compute the binding energies of transition

states (*SI Appendix*, Fig. S26). Since binding energies of transition states explicitly include the binding energy of the reactant, structure-sensitivity trends in these energies will reflect the effects of structure on both reaction intermediates and transition states. Additional details about gas phase references employed, equations used, and the structures and energies of these transition states are in *SI Appendix*. As seen in Fig. 4 E–J, we find that (211) surfaces promote these elementary steps more favorably than (111) surfaces. This promotion is observed on both clean surfaces, and surfaces containing coadsorbed CH* and OH*. Both intrinsic activation barriers and binding energies of transition states are lower on the (211) step edges compared to (111) terraces. These results strongly suggest that step-edge sites are the most active sites for propene combustion. Although metallic Pd surfaces were used in these calculations, we verified that the results held the same for metallic Pt surfaces. The experimental and theoretical investigations suggest that the promotional effect of water is observed under moderate coverages of OH*. Under these coverages, the surface exposes a multitude of undercoordinated sites without transforming into a surface oxide/hydroxide, which is inhibitory to propene combustion.

We then set out to identify the specific geometric ensemble composing the active site. The TOF for propene combustion continuously increased with increasing NP size across our library of Pd/Pt nanocrystals (Fig. 3A). We therefore expect that the number of the most active-site ensembles will follow a similar continuous increase as NP sizes increase. The active-site ensembles that we considered across a series of isostructural NPs based on Wulff construction while taking into account adsorbate–surface interactions are illustrated in Fig. 5A. The NP sizes used for this model varied from 2.8 to 8.8 nm, hence in the same range of the experimentally synthesized Pd/Pt nanocrystals. The normalized number of ensembles per surface atom for corner-kinks (CN: 6–7), step-edges (CN: 7–7), and terraces (CN: 7–8, 7–9, 8–8, 9–9) as a function of NP size was calculated and are shown in Fig. 5B. For comparison, we also report the TOF for propene combustion as a function of NP size measured experimentally at the same temperature for the Pd/Pt/Al$_2$O$_3$ catalysts with different sizes. From among the considered ensembles, only two are found to noticeably increase in fraction as the particle size increases, namely terrace sites containing two atoms with CNs of 9–9, and edge sites with CNs of 7–7. All other ensembles of sites decrease in fraction as the particle size increases, thus demonstrating that they
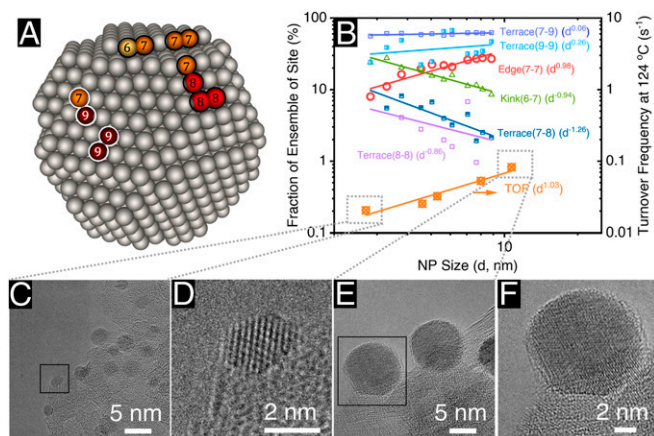

Fig. 5. (A) Definition of the ensemble of sites on Pd/Pt NP composed of 1,500 atoms (~4 nm) with color varying from yellow to red, indicating CN from low (6) to high (9). (B) Correlation between the simulated fractions of ensemble of sites and experimental TOF at 124 °C with different NP size. High-resolution TEM images of postcatalysis (C and D) 2.3-nm Pd/Pt NP and (E and F) 10.2-nm Pd/Pt NP. The boxes in C and E are used to highlight the high-resolution particles presented in D and F, respectively.

are not part of the active site, or if they are, that the reaction rate is very low. Among 9–9 and 7–7 site ensembles, the size dependency for the number of step-edge 7–7 ensembles ($d^{0.98}$) most closely corresponds to the size dependency of the experimental TOF ($d^{1.03}$). The similarity between these two functional forms explicitly indicates that edge-sites (CNs: 7–7) are the predominant undercoordinated ensembles catalyzing propene combustion. Hence, it is not the overall number of reactive sites that changes, but instead the fraction of specific reactive sites at the expense of those with lower turnover rates. The higher TOFs observed on our larger NPs can be explained because of a greater numbers of edge sites that facilitate C–C, C–H, and O–O bond dissociation, and even C–O bond formation. These edge sites are stabilized by OH* and are dynamically formed when water is cofed during propene combustion. Note that this model considers Pd and Pt atoms to be equivalent given the characterization results demonstrating that Pt maintains Pd in a metallic state (*SI Appendix*, Fig. S11). Treating Pd and Pt equally in our model makes sense for three reasons: 1) Pd remains metallic when alloyed with Pt, in contrast to pure Pd samples that show higher oxidation state; 2) the water reconstruction determines an increase in step sites for the whole particle surface, regardless of the atomic composition; 3) given the synergetic effect between Pd and Pt, it is reasonable to expect both metals contributing to the overall catalytic performance. The ab initio thermodynamic analysis further supports the second reason because $\gamma_{(211)}/\gamma_{(111)}$, which is linked to the driving force for restructuring the NP, does not strongly depend on the Pt:Pd molar ratio on the surface (*SI Appendix*, Tables S18–S21). Finally, to further support that the step sites are required for higher reaction rates, a sample consisting of 9.6-nm Pt nanocubes with mainly (100) terrace sites was synthesized and tested (*SI Appendix*, Fig. S27 *A–F*). Compared to the 10.2-nm spherical Pd/Pt NPs, the TOF on the nanocubes was about eight times lower than the on NPs (*SI Appendix*, Fig. S27*G*), which highlights the importance of step sites for high turnover rates.

Conclusions

A systematic study to identify the geometric ensemble responsible for propene combustion on Pd and Pt catalysts was conducted by using uniform catalysts and theory insights. Alumina was found to be the most active support. Among alumina-supported samples, Pt-rich catalysts were shown to deliver higher TOFs and, interestingly, to display a promoting water effect at increasing Pt content. By investigating Pd/Pt 1/1 catalysts ranging from 2.3 to 10.2 nm, we identified that the reaction is mildly structure-sensitive, with larger particles showing five times higher TOFs than smaller ones. DFT calculations were employed and undercoordinated sites on (211) stepped surfaces were found to be significantly more efficient at breaking C–H, C–C, and O–O bonds and forming C–O bonds in propene combustion compared to higher coordinated sites on (111) surfaces. Rate order measurements, together with coordination-based model calculations, demonstrated that a surface reconstruction caused by hydroxyl groups of water-created edge sites with CNs of 7–7 that were identified as the active-site ensemble for propene combustion. These insights help in the design of improved catalytic materials, in which the use of noble metals is optimized. Overall, the combination of uniform materials, computational predictions, and analysis of site stability is demonstrated as a powerful tool to identify active-site ensembles in supported heterogeneous catalysts.

Methods

Synthesis of Equimolar Pd/Pt NPs with Sizes Greater than 4 nm. Pd/Pt nanocrystals with 1/1 atomic ratio and different sizes were prepared via a seed-mediated and in situ alloying approach.

The seeds were prepared as described in our previous publication (24) (see *SI Appendix*, Table S2 for further details). The purified particles were dispersed in 6 mL of hexane and further used in the synthesis of Pd/Pt nanocrystals. For the latter, Pt(acac)$_2$ (0.125 mmol) was mixed with TOA (10 mL) in a three-neck flask. The mixture was evacuated at 80 °C for 10 min. After the flask was flushed with nitrogen, 3 mL of the Pd seed solution obtained previously (0.125 mmol of Pd) were injected into the flask. The mixture was slowly and carefully evacuated again to remove hexane and kept under vacuum for additional 10 min. Nitrogen was introduced and OLAM (1.5 mmol), OLAC (6.25 mmol), and TOP (0.066 mmol) were injected stepwise into the mixture with a 10-min degassing stage between each step. After the degassing was complete, the reaction flask was flushed with nitrogen and quickly heated (~40 °C·min^{-1}) to 250 °C. After 30 min of reaction under magnetic stirring, the solution was quickly cooled by removing the heating mantle and adding a water bath when the temperature was below ~150 °C. The particles were purified by three rounds of precipitation with a mixture of isopropanol, ethanol, and methanol, and separated by centrifugation (8,000 rpm, 3 min). Finally, the particles were dissolved in hexanes producing a deep black solution. It was found that a small volume of OLAM (50 μL) was generally needed to ensure the complete redissolution of the particles.

Catalytic Testing. To avoid thermal and mass gradients in the catalytic bed, differential conditions were maintained: catalysts were diluted with Al$_2$O$_3$ powder (<180 μm) and reactants were highly diluted (inert gas >90%), following work by Iglesia and coworker (38). Catalytic tests at different space velocities ensured that rates were obtained under strict kinetic control. For light-off curves, 30 mg of catalyst and 170 mg of alumina diluent (calcined at 900 °C for 24 h) were mixed to achieve 200 mg of powder. The 200 mg of catalyst was packed between silica sand layers inside a quartz reactor tube with an internal diameter of 10 mm mounted inside a high-temperature furnace. The sample was pretreated as follows: The catalyst was heated to 300 °C under O$_2$ (5 vol%)/Ar for 30 min, Ar for 10 min, and H$_2$ (5 vol%)/Ar for 30 min. Catalysts were cooled under Ar to 50 °C where the propene combustion reaction mixture was introduced. The reaction mixture consisted of C$_3$H$_6$ (0.15 vol%)/Ar, O$_2$ (3 vol%)/Ar, H$_2$O (10 vol%)/Ar. Gas hourly space velocity (GHSV) was held at 100,000 mL·g$_{catalyst}^{-1}$·h^{-1}, and the total flow rate was 50 mL/min. H$_2$O was introduced by heating a water saturator to 47 °C. The catalyst was then heated to 300 °C at 10 °C·min^{-1} and cooled back down to room temperature in the reaction mixture, and the gas composition was monitored using a residual gas analyzer (Hiden HPR20) and a Faraday detector following the parent molecular ions for C$_3$H$_6$ (41 amu), O$_2$ (32 amu), CO$_2$ (44 amu), and H$_2$O (18 amu).

For kinetic experiments, 10 to 40 mg of catalyst was diluted with alumina to achieve total 200 mg of powder for each test. Kinetic measurements were conducted using the same pretreatment conditions described for light-off experiments, but the final conversion was kept below 10% to ensure differential conditions. The reaction mixture was C$_3$H$_6$ (0.15 vol%)/Ar, O$_2$ (3 vol%)/Ar, H$_2$O (10 vol%)/Ar. GHSV values were held in the range of 400,000 to 800,000 mL·g$_{catalyst}^{-1}$·h^{-1} with a total flow rate of 130 mL/min. The kinetic measurements were collected above 100 °C to avoid liquid water condensation and the gas composition was measured by a gas chromatograph (Buck Scientific model 910) using flame ionization detector with a methanizer and thermal conductivity detector with Ar as the carrier gas.

The rate order measurements were all conducted below 10% conversion at constant temperature (138 ± 2 °C for Pd/Al$_2$O$_3$ and 126 ± 3 °C for the rest of the samples). The feed consisted of C$_3$H$_6$ (0.15 vol%)/Ar, O$_2$ (3 vol%)/Ar, and H$_2$O (5 vol%)/Ar, while the partial pressures of C$_3$H$_6$, O$_2$, CO$_2$, and H$_2$O were varied separately. The C$_3$H$_6$ concentration was varied between 0.1 and 0.4 vol%, O$_2$ between 1.0 and 4.5 vol%, CO$_2$ between 0 and 1 vol% and H$_2$O between 3% and 10 vol%. The rate orders of the overall reaction of propene combustion may be described by the following formula:

$$r = k P_{C_3H_6}^{\alpha} P_{O_2}^{\beta} P_{H_2O}^{\gamma}, \quad [1]$$

where r is the reaction rate; k is apparent rate constant; $P_{C_3H_6}$, P_{O_2}, and P_{H_2O} are the partial pressures of propene, oxygen, and water, respectively; and α, β, and γ are the rate order of propene, oxygen, and water, respectively.

Electronic Structure Calculations. We performed plane wave DFT calculations with the Quantum ESPRESSO package (39) within the Atomic Simulation Environment (ASE) (40). Core states were represented with ultrasoft Vanderbilt pseudopotentials (41). The Kohn–Sham equations were iteratively solved in reciprocal space on k-point grids generated using the Monkhorst–Pack scheme (42). All calculations were performed using plane-wave energy and density cutoffs of 500 and 5,000 eV, respectively. All DFT calculations on

surfaces include a dipole correction that mitigates spurious interactions between periodic images (43). Additional details such as k-points, exchange-correlation functional (44, 45), and convergence criteria for forces and energies are presented in *SI Appendix*.

Determining Barriers of C–H, C–C, and O–O Scission, and C–O Association. We calculate transition state barriers for six representative reactions from the propene combustion reaction network on Pd (211) and (111) surfaces to understand reactivity differences between edge-sites and terrace-sites. The considered reactions include CH$_2$CH–H*, CH–CH*, C–CO*, CH–C*, C–O*, and O–O*, where the bond being broken is indicated by a dash. Transition states are obtained on both pristine (211) and (111) surfaces, along with surfaces covered with 0.33 ML of CH* and OH*. CH* and OH* are representatives of coadsorbed species that likely exist on the surfaces as inferred from reaction-rate order experiments. Transition state energies are calculated using the climbing image nudged elastic band (CI-NEB) method (46). Based on the reaction, we use either six or eight intermediate images. Difficult to converge transition states are expeditiously converged using the machine-learning nudged elastic band (ML-NEB) method (47). Twenty-one images are employed in the ML-NEB calculations. All transition states are checked for the presence of a single imaginary frequency. The vibrational frequency calculations are determined from the Hessian matrix under the harmonic approximation. Additional computational details regarding gas phase references, equations used to determine thermodynamic/kinetic barriers, structures of transition states, and reactivity trends between the (211) and (111) surfaces are discussed in *SI Appendix*.

Surface Energy Calculations and Wulff Construction. We generated the morphologies of clean and OH*-covered Pd/Pt NPs using Wulff constructions. We first determined the surface energies of clean (111), (100), (211), and (110) surfaces that represent terrace and low-coordinated edge sites using symmetric slabs. To model surfaces with varying Pd:Pt ratios, we sequentially varied the compositions of the surface layer of monometallic Pt (Pd) slabs from Pt to Pd (Pd to Pt). Since the bulk atoms were either Pt or Pd for all these surface alloys, we use the appropriate monometallic lattice constant (Pt, 3.99 Å; Pd, 3.98 Å). We calculated the surface energies of (111), (100), and (110) surfaces using six-layered symmetric slabs with 2 × 2 surface supercells, while we determined surface energies of (211) surfaces using 24-layered symmetric slabs with 1 × 3 surface supercells. For the (111), (100), and (110) surfaces, we fixed the two central layers at their bulk positions, while for the (211) surface, we constrained the six central layers to their bulk positions. All other atoms were relaxed. We verified the convergence of surface energies with respect to slab thickness using 12-layered slabs for selected surfaces. Surface energies for the Pd/Pt alloys in vacuum were determined using Eq. 2:

$$\gamma_{\text{vacuum}} = \frac{E_{\text{slab}} - mE_{\text{bulk}}^{\text{Pt}} - kE_{\text{bulk}}^{\text{Pd}}}{2A},\qquad [2]$$

where γ_{vacuum} is the surface energy of the considered facet, E_{slab} is the total energy of the slab, $m(k)$ is the number of Pt (Pd) atoms in the slab, $E_{\text{bulk}}^{\text{Pt}}$ ($E_{\text{bulk}}^{\text{Pd}}$) is the total energy per atom for bulk Pt (Pd), and A is the surface area.

We determined the surface energies of OH*-covered PdPt surfaces (symmetric slabs) at the reaction temperature (423 K) and different $p_{H_2}^{0.5}$/p_{H_2O} ratios (1/100 to 100/1) using an ab initio thermodynamic approach developed by Reuter and Scheffler (48). The gas phase environment corresponds to low coverages of OH* adsorbed on the surface. OH* arises from the dissociation of water that is cofed as a reactant.

The surface energy of OH* covered surfaces was calculated using Eq. 3:

$$\gamma_{\text{OH}*} = \gamma_{\text{vacuum}} + \left[E_{ads,0}^{\text{OH}*} + \Delta ZPE - T\Delta S + kT_* \ln\left(\frac{p_{H_2}^{0.5}}{p_{H_2O}}\right)\right] \Big/ A_{111},\qquad [3]$$

where $\gamma_{\text{OH}*}$ is the surface energy of a symmetric surface slab covered with OH*, $E_{ads,0}^{\text{OH}*}$ is the ground state OH* adsorption energy predicted using site-specific scaling relations (36) (further details provided below), ΔZPE is the change in zero point energy upon adsorption, T is the temperature, ΔS is the change in entropy upon adsorption, p_{H2} and p_{H2O} are the partial pressures of H$_2$ and H$_2$O, respectively, and A_{111} is the surface area of the (111) surface to normalize the density of OH*-coverage on all surfaces, leading to a constant OH coverage of 0.25 ML on all surfaces. Vibrational frequencies were calculated from the Hessian matrix under the harmonic approximation with two displacements of 0.015 Å for each atom along each Cartesian coordinate. These frequencies were used to determine zero-point energies and entropic contributions (49). Free energies of gas-phase species were obtained using the Shomate equation with data from the NIST-JANAF Thermochemical Tables (50).

To efficiently predict adsorption energies of OH* ($E_{ads,0}^{\text{OH}*}$) on the considered surface facets of PtPd alloys with various compositions, we used site-specific scaling relations. This family of scaling relations linearly correlates adsorption energies of metal–adsorbate complexes (e.g., Pt–OH*) to stabilities of adsorption sites (e.g., Pt*) across alloys having wide-ranging morphologies and compositions (51). The adsorption site stability, which functions as descriptor in these scaling relations, is, in turn, expeditiously evaluated using a predictive alloy stability model (37, 52). The principle advantage of choosing the site stability as a descriptor is that generic changes in morphology and composition are unified within a single continuous descriptor space. We used these scaling relations to extract $E_{ads,0}^{\text{OH}*}$ from the adsorption energies of the considered metal–adsorbate complexes. Specifically, we predicted $E_{ads,0}^{\text{OH}*}$ of OH* bound on top sites located at edges (CN: 7) and terraces (CNs: 8, 9) of PtPd alloys having systematically varying surface compositions from Pt-rich to Pd-rich. Further details of this procedure are discussed in *SI Appendix*.

Using the surface energies of 1:1 Pt:Pd alloys in vacuum (Eq. 2) and under an atmosphere of $p_{H2}^{0.5}$/p_{H2O} (1/1) (Eq. 3), we generated two libraries of isostructural, Wulff-constructed NPs having sizes ranging from 3 to 9 nm. For these 1/1 Pt/Pd alloys, we used a lattice constant of 3.985 Å in accordance with Vegard's law. Since we did not geometrically optimize the structures of Wulff-constructed NPs (200 to 30,000 atoms), the specific lattice constant does not influence any trends. We determined the fraction of differently coordinated top and bridge sites per surface atom for these Wulff constructed NPs. The site densities in conjunction with kinetic measurements and surface characterization enable us to identify active-site ensembles of PtPd nanoalloys for propene combustion. A step-by-step description of the procedure for determining the surface fractions of purported active-site ensembles is provided in *SI Appendix*. These steps include predicting surface energies in vacuum, surface energies at 423 K, $p_{H2}^{0.5}$/p_{H2O} of 1/1, generating Wulff-constructed NPs, and counting adsorption sites. We have also performed a detailed sensitivity analysis of how the surface composition (Pt:Pd) ratio, OH* coverage (0.11 ML to 0.67 ML), and $p_{H2}^{0.5}$/p_{H2O} ratios (1/100 to 100/1) influence trends in surface energies. This sensitivity analysis is shown in *SI Appendix*, Tables S18–S23 and Figs. S39–S42.

Data Availability Statement. All data and methods are available within the manuscript and *SI Appendix*.

1. J. K. Nørskov et al., The nature of the active site in heterogeneous metal catalysis. *Chem. Soc. Rev.* **37**, 2163–2171 (2008).
2. M. Boudart, Model catalysts: Reductionism for understanding. *Top. Catal.* **13**, 147 (2000).
3. Z. W. Seh et al., Combining theory and experiment in electrocatalysis: Insights into materials design. *Science* **355**, eaad4998 (2017).
4. S. Chatterjee, M. Naseri, J. Li, *Heavy Duty Diesel Engine Emission Control to Meet BS VI Regulations*, (SAE International, 2017).

5. L. Styhre, H. Winnes, "Emissions from ships in ports" in *Green Ports*, R. Bergqvist, J. Monios, Eds. (Elsevier, 2019), Vol. chap. 6, pp. 109–124.
6. Q. Zhang et al., Emission factors of volatile organic compounds (VOCs) based on the detailed vehicle classification in a tunnel study. *Sci. Total Environ.* **624**, 878–886 (2018).
7. C. Akiya et al., Difference in catalytic combustion of propane and propene on Pt/Al$_2$O$_3$ catalyst. *Chem. Lett.* **28**, 801–802 (1999).

8. A. Russell, W. S. Epling, Diesel oxidation catalysts. *Catal. Rev.* **53**, 337–423 (2011).

9. M. V. Twigg, Catalytic control of emissions from cars. *Catal. Today* **163**, 33–41 (2011).

10. M. Haneda, T. Watanabe, N. Kamiuchi, M. Ozawa, Effect of platinum dispersion on the catalytic activity of Pt/Al$_2$O$_3$ for the oxidation of carbon monoxide and propene. *Appl. Catal. B* **142–143**, 8–14 (2013).

11. Z. Yang *et al.*, Size-dependent CO and propylene oxidation activities of platinum nanoparticles on the monolithic Pt/TiO$_2$-YO$_x$ diesel oxidation catalyst under simulative diesel exhaust conditions. *Catal. Sci. Technol.* **5**, 2358–2365 (2015).

12. L. M. Carballo, E. E. Wolf, Crystallite size effects during the catalytic oxidation of propylene on Ptγ-Al$_2$O$_3$. *J. Catal.* **53**, 366–373 (1978).

13. T. K. Hansen, M. Høj, B. B. Hansen, T. V. W. Janssens, A. D. Jensen, The effect of Pt particle size on the oxidation of CO, C$_3$H$_6$, and NO over Pt/Al$_2$O$_3$ for diesel exhaust aftertreatment. *Top. Catal.* **60**, 1333–1344 (2017).

14. M. Haneda, M. Todo, Y. Nakamura, M. Hattori, Effect of Pd dispersion on the catalytic activity of Pd/Al$_2$O$_3$ for C$_3$H$_6$ and CO oxidation. *Catal. Today* **281**, 447–453 (2017).

15. R. T. Vang *et al.*, Controlling the catalytic bond-breaking selectivity of Ni surfaces by step blocking. *Nat. Mater.* **4**, 160–162 (2005).

16. J. Andersin, K. Honkala, DFT study on complete ethylene decomposition on flat and stepped Pd. *Surf. Sci.* **604**, 762–769 (2010).

17. A. J. Van Strien, B. E. Nieuwenhuys, Ethylene adsorption and decomposition on platinum single crystal surfaces. *Surf. Sci.* **80**, 226–237 (1979).

18. R. T. Vang *et al.*, Ethylene dissociation on flat and stepped Ni(111): A combined STM and DFT study. *Surf. Sci.* **600**, 66–77 (2006).

19. D. Ciuparu, L. Pfefferle, Support and water effects on palladium based methane combustion catalysts. *Appl. Catal., A* **209**, 415–428 (2001).

20. R. Gholami, M. Alyani, K. J. Smith, Deactivation of Pd catalysts by water during low temperature methane oxidation relevant to natural gas vehicle converters. *Catalysts* **5**, 561–594 (2015).

21. R. Caporali *et al.*, Critical role of water in the direct oxidation of CO and hydrocarbons in diesel exhaust after treatment catalysis. *Appl. Catal. B* **147**, 764–769 (2014).

22. E. D. Goodman *et al.*, Uniform Pt/Pd bimetallic nanocrystals demonstrate platinum effect on palladium methane combustion activity and stability. *ACS Catal.* **7**, 4372–4380 (2017).

23. M. Cargnello *et al.*, Efficient removal of organic ligands from supported nanocrystals by fast thermal annealing enables catalytic studies on well-defined active phases. *J. Am. Chem. Soc.* **137**, 6906–6911 (2015).

24. J. J. Willis *et al.*, Systematic structure–property relationship studies in palladium-catalyzed methane complete combustion. *ACS Catal.* **7**, 7810–7821 (2017).

25. A. Baylet *et al.*, Parametric study of propene oxidation over Pt and Au catalysts supported on sulphated and unsulphated titania. *Appl. Catal. B* **102**, 180–189 (2011).

26. M. S. Avila, C. I. Vignatti, C. R. Apesteguía, T. F. Garetto, Effect of support on the deep oxidation of propane and propylene on Pt-based catalysts. *Chem. Eng. J.* **241**, 52–59 (2014).

27. S. Gil *et al.*, Catalytic oxidation of propene over Pd catalysts supported on CeO$_2$, TiO$_2$, Al$_2$O$_3$ and M/Al$_2$O$_3$ oxides (M = Ce, Ti, Fe, Mn). *Catalysts* **5**, 671–689 (2015).

28. Y.-H. Chin, M. García-Diéguez, E. Iglesia, Dynamics and thermodynamics of Pd–PdO phase transitions: Effects of Pd cluster size and kinetic implications for catalytic methane combustion. *J. Phys. Chem. C* **120**, 1446–1460 (2016).

29. P. Marécot *et al.*, Propane and propene oxidation over platinum and palladium on alumina: Effects of chloride and water. *Appl. Catal. B* **3**, 283–294 (1994).

30. W. D. Williams *et al.*, Metallic corner atoms in gold clusters supported on rutile are the dominant active site during water-gas shift catalysis. *J. Am. Chem. Soc.* **132**, 14018–14020 (2010).

31. M. Shekhar *et al.*, Size and support effects for the water-gas shift catalysis over gold nanoparticles supported on model Al$_2$O$_3$ and TiO$_2$. *J. Am. Chem. Soc.* **134**, 4700–4708 (2012).

32. S. Krüger, S. Vent, F. Nörtemann, M. Staufer, N. Rösch, The average bond length in Pd clusters Pd$_n$, n = 4–309: A density-functional case study on the scaling of cluster properties. *J. Chem. Phys.* **115**, 2082–2087 (2001).

33. C. J. Weststrate, I. M. Ciobîcă, A. M. Saib, D. J. Moodley, J. W. Niemantsverdriet, Fundamental issues on practical Fischer–Tropsch catalysts: How surface science can help. *Catal. Today* **228**, 106–112 (2014).

34. Z. Zhu *et al.*, Influence of step geometry on the reconstruction of stepped platinum surfaces under coadsorption of ethylene and CO. *J. Phys. Chem. Lett.* **5**, 2626–2631 (2014).

35. P. van Helden, I. M. Ciobîcă, R. L. J. Coetzer, The size-dependent site composition of FCC cobalt nanocrystals. *Catal. Today* **261**, 48–59 (2016).

36. T. S. Choksi, L. T. Roling, V. Streibel, F. Abild-Pedersen, Predicting adsorption properties of catalytic descriptors on bimetallic nanoalloys with site-specific precision. *J. Phys. Chem. Lett.* **10**, 1852–1859 (2019).

37. L. T. Roling, T. S. Choksi, F. Abild-Pedersen, A coordination-based model for transition metal alloy nanoparticles. *Nanoscale* **11**, 4438–4452 (2019).

38. J. Wei, E. Iglesia, Isotopic and kinetic assessment of the mechanism of reactions of CH$_4$ with CO$_2$ or H$_2$O to form synthesis gas and carbon on nickel catalysts. *J. Catal.* **224**, 370–383 (2004).

39. P. Giannozzi *et al.*, QUANTUM ESPRESSO: A modular and open-source software project for quantum simulations of materials. *J. Phys. Condens. Matter* **21**, 395502 (2009).

40. A. Hjorth Larsen *et al.*, The atomic simulation environment—a Python library for working with atoms. *J. Phys. Condens. Matter* **29**, 273002 (2017).

41. K. Laasonen, R. Car, C. Lee, D. Vanderbilt, Implementation of ultrasoft pseudopotentials in ab initio molecular dynamics. *Phys. Rev. B Condens. Matter* **43**, 6796–6799 (1991).

42. H. J. Monkhorst, J. D. Pack, Special points for Brillouin-zone integrations. *Phys. Rev. B* **13**, 5188–5192 (1976).

43. D. Vanderbilt, Soft self-consistent pseudopotentials in a generalized eigenvalue formalism. *Phys. Rev. B Condens. Matter* **41**, 7892–7895 (1990).

44. B. Hammer, L. B. Hansen, J. K. Nørskov, Improved adsorption energetics within density-functional theory using revised Perdew-Burke-Ernzerhof functionals. *Phys. Rev. B* **59**, 7413–7421 (1999).

45. J. Wellendorff *et al.*, Density functionals for surface science: Exchange-correlation model development with Bayesian error estimation. *Phys. Rev. B* **85**, 235149 (2012).

46. G. Henkelman, B. P. Uberuaga, H. Jónsson, A climbing image nudged elastic band method for finding saddle points and minimum energy paths. *J. Chem. Phys.* **113**, 9901–9904 (2000).

47. J. A. Garrido Torres, P. C. Jennings, M. H. Hansen, J. R. Boes, T. Bligaard, Low-scaling algorithm for nudged elastic band calculations using a surrogate machine learning model. *Phys. Rev. Lett.* **122**, 156001 (2019).

48. K. Reuter, M. Scheffler, Composition, structure, and stability of RuO$_2$(110) as a function of oxygen pressure. *Phys. Rev. B* **65**, 35406 (2001).

49. D. A. McQuarrie, J. D. Simon, *Molecular Thermodynamics*, (Sterling Publishing Company, 1999).

50. P. J. Linstrom, W. Mallard, *NIST Chemistry Webbook; NIST Standard Reference Database No. 69*, (National Institute of Standards and Technology, 2001).

51. L. T. Roling, F. Abild-Pedersen, Structure-sensitive scaling relations: Adsorption energies from surface site stability. *ChemCatChem* **10**, 1643–1650 (2018).

52. L. T. Roling, L. Li, F. Abild-Pedersen, Configurational energies of nanoparticles based on metal–metal coordination. *J. Phys. Chem. C* **121**, 23002–23010 (2017).